# Type II solar radio bursts: Modeling and extraction of shock parameters

D. S. Hillan,[1] I. H. Cairns,[1] and P. A. Robinson[1]

Received 18 April 2011; revised 24 October 2011; accepted 8 January 2012; published 16 March 2012.

[1] This first paper in a two part series summarizes the current theory and the data-driven solar wind model for simulating dynamic spectra of type II radio bursts. It also introduces performance metrics and techniques for extraction of model shock parameters from these dynamic spectra. We use an iterative downhill simplex method which compares two dynamic spectra and quantitatively assesses and improves the agreement using two figures of merit: the first is based on the correlation function and the second is based on a normalized differences over the data set. By maximizing the agreement we are able to extract the input model shock parameters to within 30% or better when using model solar winds of increasing complexity. The effects on the spectra predicted and on the figures of merit from changing the model shock parameters and solar wind model are also investigated. The iterative downhill extraction method is then applied to the type II dynamic spectrum predicted using a realistic model solar wind and a shock model estimated for an observed type II event. The shock parameters are recovered to within 10% of the correct solution.

**Citation:** Hillan, D. S., I. H. Cairns, and P. A. Robinson (2012), Type II solar radio bursts: Modeling and extraction of shock parameters, *J. Geophys. Res.*, *117*, A03104, doi:10.1029/2011JA016754.

## 1. Introduction

[2] The drifting bands of coronal and interplanetary type II radio bursts have been identified as emissions from the foreshock region of coronal or interplanetary shocks at the local plasma frequency $f_p$ (F) and its harmonic $2f_p$ (H) [*Wild*, 1950a, 1950b; *Wild et al.*, 1963; *Cane et al.*, 1982; *Cane*, 1985; *Nelson and Melrose*, 1985; *Reiner et al.*, 1998; *Robinson and Cairns*, 2000; *Bale et al.*, 1999]. These bursts often show multiple independent slowly drifting bands with bursty intensifications lasting for hours, as the emission drifts down to tens of kHz. Figure 1 shows an excellent example of an interplanetary type II burst starting on 3 December 2004. Shock-accelerated electrons in the upstream foreshock form beam distributions that are unstable to the production of Langmuir waves, that are then able to generate radio emission via nonlinear processes. A recent complete type II theory [*Knock et al.*, 2001; *Cairns et al.*, 2003; *Knock et al.*, 2003a, 2003b; *Knock and Cairns*, 2005; *Cairns and Knock*, 2006; *Florens et al.*, 2007; *Schmidt and Gopalswamy*, 2008; *Cairns*, 2011] models these processes and calculates the dynamic spectra produced by a paraboloidal shock packed with ripples moving out through a data-driven solar wind model [*Florens et al.*, 2007]. Preliminary comparisons show some qualitative and semiquantitative agreement for several observed events [*Knock et al.*, 2001; *Florens et al.*, 2007; *Schmidt and Gopalswamy*, 2008].

[3] An observed type II often appears fragmented, with bursty intensifications, and may display structure such as "split-bands," where a primary emission band is split in two, or "multiple lanes," where additional F-H bands appear with differing durations and frequency drift rates. Multiple lane events are naturally explained theoretically by the interaction of a rippled shock with a structured solar wind leading to multiple upstream source regions with differing $f_p$ [*Knock et al.*, 2003b; *Knock and Cairns*, 2005; *Cairns*, 2011]. A similar mechanism may explain split-band type IIs [*McLean*, 1967]. However, these are usually interpreted in terms of the frequency difference between source regions both upstream and downstream of a shock [*Smerd et al.*, 1974; *Vrsnak et al.*, 2002], despite the lack of any theoretical justification or definitive observational evidence [*Cairns*, 2011].

[4] Coronal mass ejections (CME) driving shocks through the corona and into the heliosphere have long been associated with interplanetary type II bursts in the kilometric range [*Wild et al.*, 1963; *Cane et al.*, 1982; *Cane*, 1985; *Nelson and Melrose*, 1985; *Reiner et al.*, 2001]. Blast waves have long been discussed as potential shock drivers in the metric type II burst range [*Cliver et al.*, 1999; *Claßen and Aurass*, 1999], but are not usually thought to persist into the interplanetary medium to drive kilometric emission [*Cane et al.*, 1987]. Similarly, it is not clear that all metric type IIs are associated with CMEs, since the metric emission does not routinely (if ever) continue smoothly to the kilometric emission of an interplanetary type II [*Cane and Erickson*, 2005]. In the foregoing type II theories, it is the presence and

[1]School of Physics, University of Sydney, Sydney, New South Wales, Australia.


0148-0227/12/2011JA016754

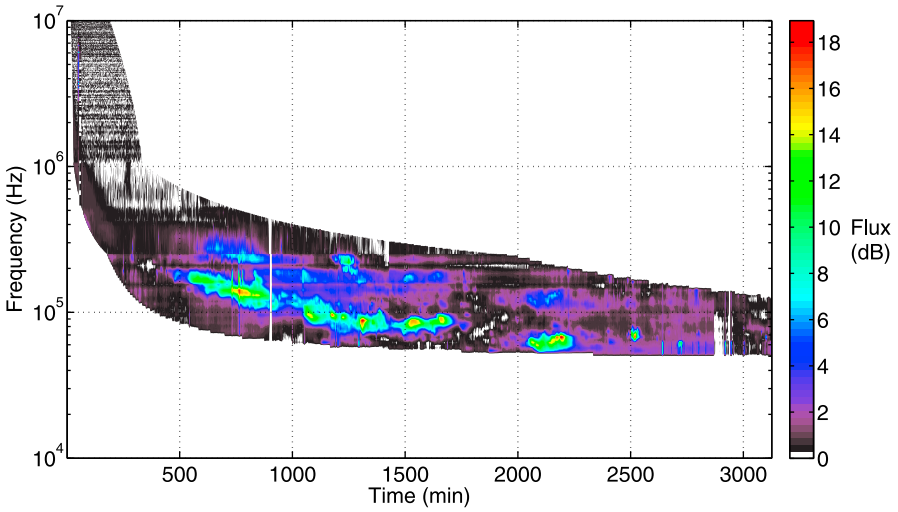


**Figure 1.** Dynamic spectrum for a well observed type II event occurring on 3 December 2004 and ending 3126 min later when the associated CME-driven interplanetary shock reached the observing Wind spacecraft. The emission tracks the plasma frequency of the source region and drifts until it reaches the plasma frequency at Earth (1 AU). The flux is in dB relative to the radio and instrumental background.

characteristics of the shock that are important, not the mechanism which produced it.

[5] The arrival of a CME-driven shock at Earth may flag the onset of geophysical effects such as auroras and geomagnetic storms, leading to technological complications for humans in orbit and on Earth. At present direct observation of CMEs with white light coronagraphs leads to shock velocity estimates [*Yashiro et al.*, 2004]. Predictions of shock arrival times based on models for CME deceleration and transit times are typically accurate to $\pm 12$ hours [*Gopalswamy et al.*, 2000, 2001, 2004]. Study of type II radio emission associated with a CME or shock event allows remote probing of the source region and may help improve our understanding of CME and shock propagation [*Dulk et al.*, 1999; *Reiner et al.*, 2001, 2007]. *Reiner et al.* [1998] used a solar wind density model to relate a type II's frequency to its heliocentric distance so as to study the lift off and arrival times of interplanetary CMEs. Similar techniques have been used by others to automatically detect type IIs and IIIs [*Lobzin et al.*, 2010] and also to probe the density structure of the deep corona [*Lobzin et al.*, 2009; *Cairns et al.*, 2009]. Since the type II dynamic spectrum is predicted to depend sensitively on the time-varying three-dimensional shock location and velocity and on the solar wind plasma [*Knock and Cairns*, 2005; *Cairns and Knock*, 2006; *Florens et al.*, 2007], a long-term vision is that iterative comparisons of type II data and theoretical predictions will yield the time-varying location and velocity of the CME-driven shock. This would allow assessment of whether, when, and with what Alfven Mach number the three-dimensional shock might reach Earth's magnetosphere.

[6] This paper is the first of a pair that uses the recently developed type II theory to investigate type II solar radio burst events and their associated macroscopic shock characteristics. They also provide the first detailed quantitative tests of the type II theory. This paper summarizes the recent type II theory and the associated data-driven model for the solar wind, and then shows that the shock parameters can be robustly extracted by iteratively comparing theoretical predictions with simulated observations. This supports the vision above that data-theory comparisons of type II do have significant potential for predicting shock arrival times at Earth and associated space weather predictions. The companion paper (D. Hillan et al., Type II solar radio bursts: 2. Comparison of type II theory with observation, submitted to *Journal of Geophysical Research*, 2011) then compares theoretical predictions with observed type II events, demonstrates reasonable quantitative agreement, and constrains shock parameters.

[7] The paper is organized as follows. Section 2 summarizes in detail the data-driven solar wind model, type II theory, and the "simplex" iterative minimization method. Section 3 introduces two ways in which we can quantify the agreement between two type II dynamic spectra. Section 4 applies the simplex method to type II predictions for three model solar winds of increasing complexity and demonstrates how the shock parameters are extracted accurately. Section 5 investigates the relationship between the shock parameters and the simulated dynamic spectra, and hence the effect on the two measures of agreement. Section 6 applies the parameter extraction method to a realistic type II dynamic spectrum calculated for a real structured solar wind. The results are summarized in section 7.

## 2. Theoretical Model

[8] The theoretical model of *Knock et al.* [2001], *Cairns et al.* [2003], *Knock et al.* [2003a, 2003b], *Knock and Cairns* [2005], *Cairns and Knock* [2006], *Florens et al.* [2007], and *Schmidt and Gopalswamy* [2008] predicts the source of the type II radio emission to lie in the foreshock region (between the curved shock front and its tangential magnetic field lines) upstream of a MHD shock front. The qualitative steps in the model are (1) a rippled shock front expands out into a solar wind model based on measurements at 1 AU, (2) electrons are reflected and accelerated by the shock, with electron beams naturally forming due to time-of-flight effects, (3) the

non-zero convective derivative of the available energy in the velocity distribution leads to growth of Langmuir waves, and (4) Langmuir waves undergo nonlinear decay and coalescence to produce radio emission at the local plasma frequency and its harmonic, described by known conversion efficiencies. The model relies on analytic theory describing the above processes, along with knowledge of the shock's location and velocity and the solar wind plasma parameters. A recent review by *Cairns* [2011] summaries the theoretical assumptions made and gives a comprehensive review of the work and theories in the field to date. Only a brief summary of the theoretical model is given here.

[9] We start with a paraboloidal shock that is closely packed with ripples whose individual radii of curvature $r_c$ depend on the local spatially varying decorrelation length of the magnetic field $L(h)$, where $h$ is the heliocentric distance [*Knock et al.*, 2003b; *Neugebauer and Giacolone*, 2005]. They are packed onto the macroscopic shock with azimuthal symmetry about the shock's velocity vector but with different ripples in the eastern and western hemispheres. The ripple parameters are determined by the wind properties in the ecliptic plane. The ripple lifetime is $\tau_r = r_c/V_A$ where $V_A$ is the Alfven speed and the ripple's radius of curvature $r_c(h)$ obeys [*Knock et al.*, 2003b; *Cairns and Knock*, 2006]

$$r_c(h) = 10^9 \left(\frac{r}{1\ \mathrm{AU}}\right)^{1.61}. \quad (1)$$

Solar wind variability occurs on the scale of the ripples and their separation, so the plasma parameters must be specified everywhere upstream of the model shock.

[10] A two-dimensional data-driven solar wind model is used to create a snapshot of the solar wind over a full solar rotation period (27 days) [*Florens et al.*, 2007]. Data from the SWE and MFI instruments onboard Wind provide the observations at 1 AU. The number density $n$, electron and ion temperatures $T_e$ and $T_i$, flow velocity $\mathbf{v_{sw}}$, and magnetic field $\mathbf{B}$ are extrapolated Sunwards assuming persistence of the solar wind sources and structures during one solar rotation period. The mapping relates the time of observation to the heliolongitude of the source on the Sun using $\mathbf{v_{sw}}$. For a radial flow ($\mathbf{e_r}$) starting from the Sun's surface ($R_s$, $\phi_s$) with conserved electron number and speed, power law-like relations are used to map the velocity and density as functions of heliocentric distance $r$ and longitude $\phi$ in the ecliptic plane

$$v_{sw}(r,\phi) = v(R_s,\phi_s)\mathbf{e_r}, \quad (2)$$

$$n(r,\phi) = n(R_s,\phi_s)\left(\frac{R_s}{r}\right)^2. \quad (3)$$

The electron and ion temperatures are given by

$$T_e(r,\phi) = T_{es}(R_s,\phi_s)\left(\frac{R_s}{r}\right)^{0.42}, \quad (4)$$

$$T_i(r,\phi) = T_{is}(R_s,\phi_s)\left(\frac{R_s}{r}\right)^{0.67}. \quad (5)$$

Similarly, Parker-like magnetic field solutions define the magnetic field components in the solar wind to 1 AU [*Florens et al.*, 2007]. The field magnitude and direction vary with $\phi$ and $r$, with the direction determined by the 1 AU data. Therefore, $\mathbf{B}$ is not necessarily along the nominal Parker spiral. This model is thus a cylindrical 2D ($r$, $\phi$, $z$) model of the solar wind with the plasma parameters identical for all coordinates $z$ out of the ecliptic plane for a given ($r$, $\phi$).

[11] With the solar wind parameters specified upstream in the foreshock of each ripple, the radio emission is calculated via four steps [*Knock et al.*, 2001]:

1. A $\kappa$ distribution is used to model the nonthermal solar wind electron distribution function for speeds perpendicular and parallel to the magnetic field ($v_\perp$ and $v_\parallel$):

$$f_\kappa(v_\parallel, v_\perp) = \frac{n_0\Gamma(\kappa+1)}{\Gamma(\kappa-1/2)}\pi^{-3/2}V_e^{-3}\left(1+\frac{v_\parallel^2+v_\perp^2}{V_e^2}\right)^{-(\kappa+1)}. \quad (6)$$

An exponent value of $\kappa = 3$ is assumed for modeling the solar wind [*Maksimovic et al.*, 1997]. The incident distribution is therefore defined throughout the foreshock using (6). Electrons are accelerated and reflected at the shock front. The minimum perpendicular speed for an electron to be reflected for a given $v_\parallel$ is

$$v_{\perp c}^2(v_\parallel, v_\perp) = \frac{(v_\parallel^{HTF})^2 + \frac{2}{m}e\Delta\Phi'}{B_2/B_1 - 1}, \quad (7)$$

where $\Delta\Phi'$ is the cross-shock potential [*Kuncic et al.*, 2002] and $v_\parallel^{HTF}$ is the parallel speed in the de Hoffman-Teller frame, in which there is no motional electric field. Integrating (6) over perpendicular velocity gives the incident distribution as a function of foreshock location

$$F_\kappa(v_\parallel, R, x) = 2\pi\int_0^c v_\perp f_\kappa(v_\parallel, v_\perp)dv_\perp, \quad (8)$$

where $c$ is the speed of light.

2. The reflected electron distribution is found by integrating (6) over those perpendicular velocities which are not lost downstream:

$$F_\kappa(v_\parallel, R, x) = 2\pi\int_{v_{\perp c}}^c v_\perp f_\kappa(v_\parallel, v_\perp)dv_\perp. \quad (9)$$

Each element of the reflected distribution upstream is mapped to a location on the shock via Liouville's theorem. The incident parallel velocity in the solar wind frame (SWF) is related to the reflected parallel velocity in the rest frame of the macroscopic shock (SRF), such that

$$v_{\parallel_r}^{SWF} = -v_{\parallel_r}^{SRF} - 2V_\parallel^{WH} + U\cos\theta_{\mathrm{UB}}, \quad (10)$$

where $V_\parallel^{WH}$ is the speed of the solar wind relative to the HTF, $U$ is the upstream plasma speed, and $\theta_{UB}$ is the angle between the velocity $\mathbf{U}$ and $\mathbf{B}$ [*Filbert and Kellogg*, 1979; *Cairns*, 1986, 1987a, 1987b].

3. The electron beams present in the distribution function lead to the growth of Langmuir waves. The distribution function flattens and approaches marginal stability as the available free energy drives Langmuir waves. Fluctuations in the ambient medium allow the waves and electrons to fluctuate about marginal stability, with net energy from electrons to waves as the electrons move away from shock,

as described by stochastic grown theory (SGT) [*Robinson*, 1992; *Robinson et al.*, 1993; *Robinson and Cairns*, 1993; *Cairns and Robinson*, 1999]. Quasi-linear relaxation is used to estimate the available free energy for Langmuir growth with the beam number density $N_b$, speed $v_b$, and width $\Delta v_b$ determined from (6)–(10). The power flux into the Langmuir waves is then given as the convective derivative of the available free energy $\approx (v_b \nabla N_b m_e v_b^2 \frac{\Delta v_b}{v_b})/3$. The factor of 3 comes from quasi-linear theory [e.g., *Melrose*, 1985]. The gradient $\nabla$ is approximated by $r^{-1}$, where $r$ is the distance from the shock along the path of particles with $v_{\|} = v_b$.

4. Radio emission at $f_p$ ($F$) and $2f_p$ ($H$) is created by specific nonlinear wave processes [*Cairns and Melrose*, 1985; *Melrose*, 1985; *Cairns*, 1988; *Robinson and Cairns*, 1993]. Beam-driven Langmuir waves $L$ are subject to the electrostatic decay $L \rightarrow L' + S$, which produces backscattered Langmuir waves $L'$ and ion acoustic waves $S$. Harmonic emission then proceeds via the standard coalescence $L + L' \rightarrow T(2f_p)$. Fundamental emission proceeds via the electromagnetic decay $L \rightarrow T(f_p) + S'$, stimulated by the $S$ waves produced by the electrostatic decay. Other emissions processes are possible. Presently the theory does not include fundamental emission by linear mode conversion of Langmuir waves at density gradients [e.g., *Kim et al.*, 2007] or antenna radiation from Langmuir eigenmodes [*Ergun et al.*, 2008] or other localized Langmuir wave packets near either $2f_p$ [*Malaspina et al.*, 2010] of $f_p$. More discussion can be found elsewhere [*Cairns*, 2011].

[12] Combining the known conversion efficiencies of Langmuir to radio waves $\phi_M$ (where $M = F$ or $M = H$ for fundamental and harmonic emission, respectively) with the SGT prediction for the net energy transfer to Langmuir waves leads to the volume emissivity

$$j_M \approx \frac{\phi_M}{\Delta\Omega_M} \frac{N_b m_e v_b^3}{3r} \frac{\Delta v_b}{v_b}, \tag{11}$$

with

$$\phi_F \approx 72\sqrt{3} \frac{\gamma_{L'}}{\gamma_S} \frac{V^3}{c^3} \frac{v_b}{\Delta v_b} \frac{e^{-u_c^2}}{u_c\sqrt{\pi}} \zeta_F, \tag{12}$$

$$\phi_H \approx \frac{18\sqrt{3}}{5\gamma} \sqrt{\frac{m_i}{\gamma m_e}} \frac{v_b^2 V^3}{c^5} \frac{v_b}{\Delta v_b} \zeta_H, \tag{13}$$

where $\Omega_M$ is the solid angle over which the emission is spread, and $\gamma = 1 + 3T_i/T_e$ [*Robinson and Cairns*, 1998a, 1998b]. Further details on (11)–(13) are found in the work of *Robinson and Cairns* [1998b]. Definitions can be found there of the terms $\zeta_F$ and $\zeta_H$, which are the fractions of Langmuir waves contributing to the radio emission, and $\gamma_{L'}/\gamma_S$, which is the ratio of the damping rates of ion sound waves $S$ and backscattered Langmuir waves $L'$ produced by the electrostatic decay $L \rightarrow L' + S$ and available to stimulate fundamental emission via the process $L \rightarrow T + S$.

[13] The flux from each foreshock volume element at each ripple is summed over the macroscopic shock at each time step $\tau_r$ [*Knock et al.*, 2003b; *Cairns and Knock*, 2006] leading to a theoretical dynamic spectrum at an observer $\mathbf{r_o}$. The flux density of radiation $F_M$ into the mode $M$ assuming straight line propagation and an inverse square falloff with distance is

$$F_M(f, t, \mathbf{r}_o) = \sum_{t'} \frac{\Delta\Omega_M}{\Delta f} \int d^3V \frac{j_M(f, t', \mathbf{r})}{|\mathbf{r} - \mathbf{r}_o|^2}, \tag{14}$$

where [*Cairns*, 2011]

$$t = t' + |\mathbf{r} - \mathbf{r}_o|/c. \tag{15}$$

We use a right handed Cartesian coordinate system where $R$ lies along the tangential magnetic field line with $x$ and $z$ perpendicular [*Cairns*, 1987b], and hence the volume element in (14) is $V = R_\epsilon x_\epsilon z_\epsilon$ [*Knock et al.*, 2003a, 2003b].

[14] The focus of the macroscopic paraboloidal shock moves directly along the Earth - Sun line and has an initial radial speed $v_i$, starting at 1.1 solar radii ($R_\odot$), with constant linear deceleration $a$. The assumption of a linear acceleration profile is an easy and simple model of CME evolution that relies on the initial speed $v_i$ and the estimated event length, sufficient for the first quantitative comparisons of our model and observation (D. Hillan et al., submitted manuscript, 2011). However, some observations show non-constant deceleration or periods of zero deceleration [*Gopalswamy et al.*, 2001; *Reiner et al.*, 2007].

[15] In the $R$-$x$ plane the equation for the shock location is

$$G(R, x) = \frac{x}{\sin\theta_{UB}} + \frac{(-R\sin\theta_{UB}, + x\cos\theta_{UB})^2}{R_c} = 0, \tag{16}$$

where $\theta_{UB}$ is the angle between the upstream plasma flow and the local upstream magnetic field and $R_c$ is the radius of curvature of the macroscopic paraboloidal shock. It is assumed that $R_c$ evolves with the heliocentric distance $h$ of the shock's focus according to

$$R_c(h) = s\left(\frac{h}{1\ \mathrm{AU}}\right)^{d+1}, \tag{17}$$

where $s$ is the shock's radius of curvature at 1 AU and $d$ is the expansion index.

[16] The theory predicts that the emitted radiation's intensity and frequency-time structures depend sensitively on the shock's 3D location, velocity, and (upstream) emitting volume and associated solar wind parameters, and not just on the shock speed. Two reasons are that the emitted flux for each ripple or for the macroscopic shock depend on the respective radius of curvature squared [i.e., *Knock et al.*, 2003a, Figure 7] and that specific frequency-time components are only produced when the relevant solar wind regions are within the shock's emission volume [i.e., *Knock and Cairns*, 2005, Figures 5–9; *Cairns and Knock*, 2006, Figures 5–6]. The macroscopic shock's radius of curvature $R_c$ and emission volume depend on $s$, $d$, and $h$ via (17) while the local ripple radius of curvature $r_c(h)$ varies with $h$ according to (1). In addition, the time-evolving shape of the macroscopic shock will alter the local angle $\theta_{UB}$ of a ripple while changing the shock's velocity/acceleration profiles will alter the relative velocity between each ripple

and the local solar wind. These effects will change the predicted flux levels because more quasi-perpendicular and faster shocks have been shown to increase the observed flux [*Knock et al.*, 2003a]. Similarly, larger radii of curvature will lead to more intense, broader bandwidth emission because more regions of the solar wind conducive to radio emission will be encountered; conversely narrow shocks with smaller $R_c$ will lead to weaker and more narrow band emission [*Knock et al.*, 2003a]. Finally, localized solar wind structures within the active emission volume upstream of the shock are responsible for much of the variability and structure in the radio emission [*Reiner et al.*, 2001; *Cairns et al.*, 2003; *Knock and Cairns*, 2005; *Cairns and Knock*, 2006; *Florens et al.*, 2007]. Accordingly $V_i$, $s$, $d$, and a model for the inhomogeneous solar wind plasma are all important quantities for a truly quantitative theory of type II emission that attempts to describe and fit the levels and fine structures in observed dynamic spectra, as proposed here. Note that empirical estimation of shock speeds from $f - t$ traces in dynamic spectra do not contain information only on the radial shock speed (as assumed sometimes [e.g., *Reiner et al.*, 1998]) but also on the motion of the active emission elements (e.g., ripples) across the shock surface [*Knock and Cairns*, 2005; *Hoang et al.*, 2007].

[17] Integrating over the global emission volume yields the predicted type II intensity $T(t, f)$ as a function of time and frequency at a distant observer (in SI units of W $m^{-2}$ $Hz^{-1}$ $sr^{-1}$). The Wind/WAVES data are conventionally displayed in decibels (dB) of the total intensity relative to the minimum total daily background (instrument and natural signals) [*Bougeret et al.*, 1995; *Reiner et al.*, 1998; *Bale et al.*, 1999; *Cane and Erickson*, 2005; *Reiner et al.*, 2007]. Here, while subtraction of the background from the observations [*Hoang et al.*, 2007] followed by comparison with $T(t, f)$ would also be a viable approach, the standard Wind/Waves approach is adopted. That is, a detailed model for the intensity $B(f)$ of background signals is added to $T(t, f)$, and this combined intensity is then divided by $B(f)$ and converted into dB. In this way, the observations remain unaltered, the effects of the instrumental and natural backgrounds on the observability of the type II radiation are included, the analyses are performed with data that are routinely and rapidly available (as desired for the desired space weather applications), and both the data and theoretical predictions are given in dB as type IIs are typically weak compared with the observed satellite background.

[18] The background model of *Hillan et al.* [2010, Figure 13] is used to predict $B(f)$ as a function of frequency (in W $m^{-2}$ $Hz^{-1}$) over the entire frequency range of the Wind/WAVES instrument (4-13825 kHz [*Bougeret et al.*, 1995]). This model includes contributions from galactic background radiation, dominant at high frequencies above around 300 kHz, local quasi-thermal plasma noise, dominant at low frequencies below around 300 kHz, and receiver noise. Now $B(f)$ is added to the theoretical flux $T(t, f)$, with a time resolution of 1 minute for all 550 frequency channels. The channel frequency spacing varies with the three receivers that span the Wind/WAVES frequency range. However, in the range where much of the observed type II emission occurs (typically $\approx 20$ kHz $-$ 1 MHz), the frequency spacing is normally no greater than 4 kHz [*Bougeret et al.*, 1995; *Hillan et al.*, 2010]. We convert the flux of the dynamic spectrum into a relative decibel scale using

$$T_B(t, f) = 10\log[(\mathrm{T(t,f)} + \mathrm{B(f)})/\mathrm{B(f)}], \tag{18}$$

where $T_B(t, f)$ is the dynamic spectrum in relative flux units (dB). These dynamic spectra may be directly compared with those measured by Wind/WAVES and accessible from and reported by the Wind/WAVES team [e.g., *Bougeret et al.*, 1995; *Reiner et al.*, 1998, 2001, 2007]. All simulation results presented in this paper are in these units. Future work should evaluate the effects of the logarithmic compression into a dB scale and the possible benefits of converting the observations into calibrated absolute units intensities and then performing the theory-data comparisons.

[19] We wish to constrain the time-varying shock parameters by searching for the best agreement between theory and data. This search may be performed iteratively through a downhill simplex optimization or "Amoeba" method [*Nelder and Mead*, 1965; *Press et al.*, 1992]. Generally, these type of methods work by first defining a starting simplex of vertexes, where estimates of the shock parameters form the vertexes and the associated minimization parameter is known at each vertex, and second the algorithm attempts to track downhill in a N-dimensional space by choosing new vertexes that reduce the minimization parameter. We use the following five steps:

1. A simplex is created where the initial vertexes are randomly chosen in a plausible parameter range. The number of vertexes is equal to the number of fitted parameters plus one.
2. Simulations are performed with these vertex parameters.
3. Simulated dynamic spectra are compared with the "observational" dynamic spectrum with which we are trying to obtain agreement, yielding a quantitative figure of merit.
4. This figure of merit is iteratively optimized via the Amoeba algorithm by revising the vertexes and repeating steps 3 and 4, until the figure of merit at the vertexes differs by no more than 5%.
5. Steps 1–4 are repeated multiple times with new randomly chosen vertexes to ensure that the scheme finds the global minimum and does not settle on local minima, which may exist for certain choices of initial vertexes. The differences in the parameter values of the final simplex allow us to estimate the uncertainty.

## 3. Quantifying Agreement

[20] Two methods of calculating a quantitative figure of merit for the theory-data comparisons are discussed below. The results in sections 4 to 6 demonstrate that these figures of merit are effective in conjunction with the simplex optimization method.

### 3.1. $\alpha$ Parameter

[21] The images of the theoretical and observed dynamic spectra may be compared by cross correlating the two data sets to ascertain the level of agreement. For example,

$$C(t,f) = (DB_O \star DB_T)(t, f) = \int_f \int_t DB_O(t, f) DB_T(t+\tau, f+\rho) d\rho d\tau, \tag{19}$$

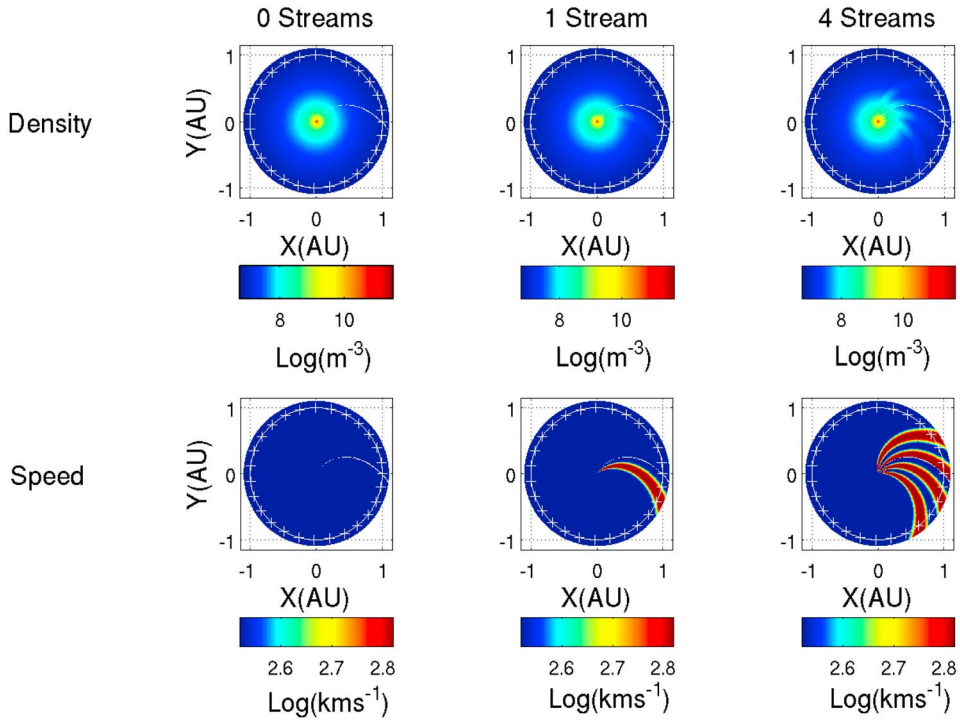


**Figure 2.** (top) Density and (bottom) speed plotted for the three solar wind models; (left) 0 streams (isotropic), (middle) 1 stream, and (right) 4 streams.

where $DB_O(t, f)$ is the observed dynamic spectrum, $DB_T(t + \tau, f + \rho)$ is the model dynamic spectrum, $t$ and $f$ correspond to the time and frequency indexes, respectively, and $\rho$ and $\tau$ are variables of integration. A normalized 2-D cross-correlation of two data sets of size $n$ by $m$ yields an array of correlation coefficients of size $2n$-1 by $2m$-1 whose magnitudes range from $-1$ to 1. A perfect match between data sets corresponds to the maximum correlation coefficient $C_{\max} = 1$ occurring in the center of the correlation array at $(t, f) = (0, 0)$. If two initially identical data sets are cross-correlated after one is translated by $(x, y)$, then the correlation array will contain $C_{\max} = 1$ at the point $(x, y)$ relative to the center at (0,0).

[22] We may use the offset $(t_0, f_0)$, where $t_0$ and $f_0$ label the indexes in time and frequency, of the position of $C_{\max}$ in the array formed by correlating images of dynamic spectra to calculate

$$\alpha = \sqrt{\left(\frac{t_0}{n}\right)^2 + \left(\frac{f_0}{m}\right)^2}. \tag{20}$$

This quantity $\alpha$ is a dimensionless measure of the distance the two images are offset and must be translated to attain maximal agreement. The minimum possible value $\alpha = 0$ corresponds to a perfect aligning of features in the two data sets. The maximum possible value $\alpha = 1$ corresponds to an alignment of features when one data set is translated by the entire grid size in both time and frequency. The value of $C_{\max}$ also determines the strength of the agreement, with values close to one meaning better agreement. The values of $\alpha$ and $C_{\max}$ are independent measures of agreement between the two data sets. Here we consider $\alpha$ only for the iterative scheme, since there does not appear to be a unique way of combining $\alpha$ and $C_{\max}$ into a single quantity. The value of $C_{\max}$ for the minimum $\alpha$ is then an independent estimate of how well the two images agree.

### 3.2. $\beta$ Parameter

[23] We define a parameter $\beta$ which sums the differences in relative flux levels between an observed and a theoretical dynamic spectrum at each point:

$$\beta = \sum_{i=1}^{n} \sum_{j=1}^{m} \frac{|DB_{Ti,j} - DB_{Oi,j}|}{DB_{Ti,j} + DB_{Oi,j}}, \tag{21}$$

where $n$ and $m$ are the numbers of time and frequency points, respectively. When $\beta$ is equal to zero, the relative flux levels have zero difference at all points and the data sets are identical. Reducing $\beta$ therefore minimizes the differences in relative flux over the data sets, and should improve the match. Note the $\beta$ parameter measures the normalized deviation between the two data sets. This is arguably a more robust parameter than the $\chi^2$-statistic [*Press et al.*, 1992], since the probabilistic interpretation of the $\chi^2$ statistic requires the deviations to be normally distributed which is n often not the case. For instance, in another context, *Zarka et al.* [2004] show that the galactic background and receiver noise observed by the Cassini Radio and Plasma Wave Science instrument at 1.075 MHz is not Gaussian. *Zarka et al.* [2004, Figure 3c] shows a two clear peaks near the core and significantly non-Gaussian tails. In addition, the errors or uncertainties in the predicted type II dynamic spectrum relate to, for instance, the different positions of ripples

**Table 1.** Plasma Parameters at 1 AU for the Isotropic Artificial Solar Wind Model and the Stream Variations for the 1 and 4 Stream Solar Wind Models

| Parameter | Isotropic Value | Stream Variation |
|---|---|---|
| Density ($cm^{-3}$) | 7 | 10 |
| Speed ($km\ s^{-1}$) | 330 | 660 |
| Magnetic field (T) | $4.5 \times 10^{-5}$ | $1.1 \times 10^{-5}$ |
| Electron temperature (K) | $1.5 \times 10^{5}$ | $1.5 \times 10^{5}$ |
| Ion temperature (K) | $5 \times 10^{4}$ | $1 \times 10^{5}$ |

**Table 2.** Amoeba Starting Simplex Parameter Ranges for Testing Recovery of Three Free Parameters[a]

| Parameter | Minimum | Maximum |
|---|---|---|
| $v_i$ ($km\ s^{-1}$) | 1200 | 1900 |
| $s$ | 0.1 | 2.0 |
| $d$ | 0.00 | 1.00 |

[a]The columns list the minimum and maximum ranges for the randomly chosen parameters at each vertex.

between iterations (and even between the Amoeba vertices for a given iteration). These errors are also not expected to be normally distributed.

## 4. Extracting Shock Parameters in a Simple Model Solar Wind

[24] We model three artificial solar winds of gradually increasing complexity in order to test the parameter extraction method. The first is a constant solar wind with no azimuthal or polar variations in parameters, the second contains one stream of hotter, higher density, and higher speed wind extending toward Earth, and the third contains four of these streams evenly spread around the Sun-Earth line in the Earth-facing quadrant. The velocity and density maps for these three models are illustrated in Figure 2, with the specific plasma parameters for the isotropic wind and fast streams defined at 1 AU in Table 1. We then take a nominal shock with parameters $v_i$ = 1500 km $s^{-1}$, $a$ = −4.2 m $s^{-2}$, $s$ = 1.0, and $d$ = 0.37 in (17) and produce the dynamic spectra for the three wind models for future testing of the recovery of shock parameters. These reasonable shock parameters form our "canonical" simulation parameters in all sections below. The three spectra for the zero stream, one-stream, and four-stream solar wind models are shown in Figure 3 in the first row of columns 1, 2, and 3, respectively, leading to distinct bands of fundamental (lower) and harmonic (upper) emission. At a glance it is clear that solar wind structures significantly affect the dynamic spectrum, as found previously [*Knock and Cairns*, 2005; *Cairns and Knock*, 2006; *Florens et al.*, 2007]. The differences between the fundamental and harmonic emission bands are also observed to increase as the solar wind model becomes more structured. This is consistent with the differing upstream plasma parameter dependencies for the fundamental and harmonic emission in (12) and (13), respectively.

[25] Iterative fitting by the Amoeba method for the dynamic spectra calculated for a specific artificial solar wind model and shock model is performed as outlined at the end of section 2. The initial vertexes are chosen in the ranges listed in Table 2. The figure of merit calculated for each

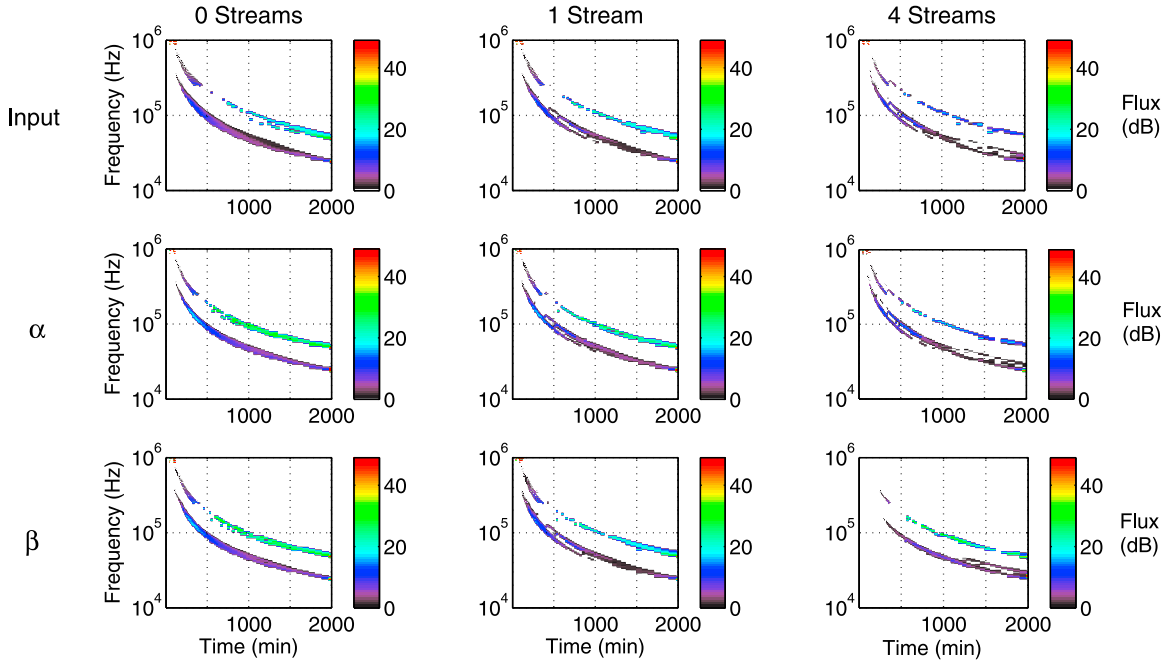


**Figure 3.** (top) Simulated type IIs produced using the model shock parameters $v_i$ = 1500 km $s^{-1}$, $a$ = −4.2 m $s^{-2}$, $s$ = 1.0 and $d$ = 0.37 and the model solar wind with no streams (left), 1 stream (center), and 4 streams (right). (middle) Dynamic spectra resulting from extracting shock parameters using the $\alpha$ assessment parameter for the three solar wind models. (bottom) Dynamic spectra resulting from extracting shock parameters using the $\beta$ assessment parameter for the three solar wind models. See Table 3 for the extracted parameters.

**Table 3.** Amoeba Results for the Three Solar Wind Models Using the Two Assessment Parameters[a]

| | Parameters | | | | Results | | | |
|---|---|---|---|---|---|---|---|---|
| Method | $v_i$ | $a$ | $s$ | $d$ | $C_{max}$ | $(t_0, f_0)$ | $\alpha$ | $\beta$ |
| | | | | *0 Streams* | | | | |
| $\alpha$ | 1549 ± 22 | −5.0 | 1.25 ± 0.06 | 0.31 ± 0.04 | 0.32 | (0,0) | 0.00 | $2.38 \times 10^4$ |
| $\beta$ | 1563 ± 23 | −5.3 | 1.25 ± 0.05 | 0.33 ± 0.05 | 0.35 | (19,0) | $9.5\times 10^{-3}$ | $2.40 \times 10^4$ |
| | | | | *1 Stream* | | | | |
| $\alpha$ | 1565 ± 3 | −5.3 | 1.25 ± 0.01 | 0.34 ± 0.01 | 0.28 | (0,0) | 0.00 | $2.48 \times 10^4$ |
| $\beta$ | 1635 ± 41 | −6.5 | 1.00 ± 0.11 | 0.47 ± 0.08 | 0.28 | (15,0) | $7.50\times 10^{-3}$ | $2.55 \times 10^4$ |
| | | | | *4 Streams* | | | | |
| $\alpha$ | 1610 ± 1 | −6.1 | 1.09 ± 0.01 | 0.42 ± 0.01 | 0.25 | (0,0) | 0.00 | $2.71 \times 10^4$ |
| $\beta$ | 1500 ± 13 | −4.3 | 1.43 ± 0.05 | 0.20 ± 0.03 | 0.26 | (66,1) | $3.30\times 10^{-2}$ | $2.49 \times 10^4$ |

[a]Each row lists, from left to right, the assessment parameter used, the parameters extracted, and the values of each assessment parameter.

vertex and at each iteration is either the $\alpha$ or $\beta$ parameter described in section 3.1 and 3.2, respectively. The three parameters fitted are $v_i$, $s$, and $d$.

[26] The results for recovering the three free parameters $v_i$, $s$, and $d$ for the shock model are shown in Figure 3 and Table 3, where both the parameters and the calculated values of $\alpha$, $\beta$, and $C_{max}$ are listed. Furthermore, the value of acceleration $a$ is given, although this is not independent but instead constrained by the event length and the initial velocity $v_i$. The input shock model has $v_i$ = 1500 km s$^{-1}$, $a$ = −4.2 m s$^{-2}$, $s$ = 1, and $d$ = 0.37; hence Table 3 shows that both methods successfully recover the shock's speed to within 5% or better. The shock size $s$ and expansion index $d$ are only extracted to within 30% or better, with on average a larger shock size on average $s \approx 1.3$ and smaller expansion index $d \approx 0.35$ recovered, relative to the true values. Note that the $\alpha$ minimization technique leads to zero time and frequency offsets in these cases, but that the $\beta$ technique does not. However, the largest $\beta$ offset is (66, 1) corresponding to 66 min and 4 kHz, which is 3% of the event duration (2000 min) and 1% of the characteristic frequency range (≈ 1 MHz), respectively. Figure 4 compares the shock evolution for the input parameter set and for the best recovered model shock solutions for the $\alpha$ and $\beta$ minimizations. Figure 4 indicates that the recovered shock parameters lead to model shocks that track the correct solution very closely, especially near the nose of the shock.

## 5. Sensitivity of Fitting Parameters

[27] When comparing two dynamic spectra the differences may include the relative flux levels, the presence of features such as bands and bright spots, and the time and frequency at which these features occur. It is important to understand how to quantify the agreement between spectra that have such differences.

### 5.1. Effect of Differing and Offset Relative Flux Levels

[28] To investigate the effect of data sets that differ only by their relative flux level we take the dynamic spectra $DB_T(t, f)$ predicted for the four-stream model solar wind with the nominal shock parameters (Figure 3, top right) and multiply it by a constant dimensionless factor $A$. Using $DB_T(t, f)$ and $AT_B(t, f)$ we calculate $\alpha$ and $\beta$ and hence quantify the agreement between them. Figure 5 shows how $\alpha$ and $\beta$ change with $A$ between 1 and 10. It is seen that the correlation function analysis used to calculate $\alpha$ is insensitive to changes in the relative flux levels. As long as the relative features in the images are constant, $\alpha$ will remain close to the value for $A$ = 1 (equal to zero in this case). Changes in relative flux levels affect the $\beta$ parameter by

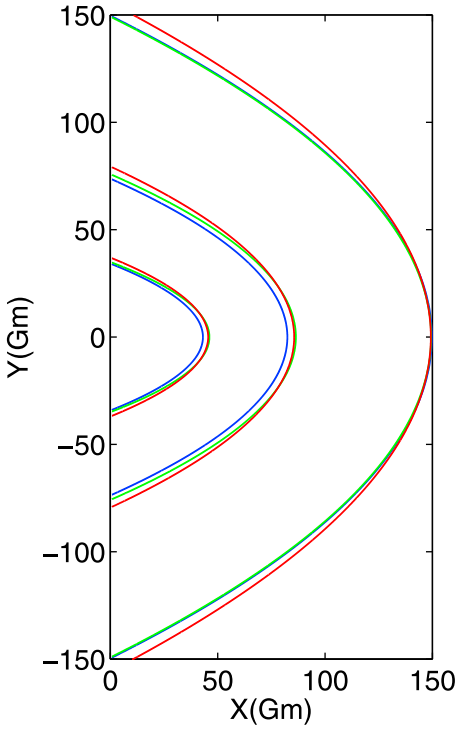


**Figure 4.** Shock locations at times $t$ = 500 min, $t$ = 1000 min, and $t$ = 2000 min from left to right for the input shock and the two best extracted solutions. Blue lines show the shock locations at these times for the input shock parameters: $v_i$ = 1500 km s$^{-1}$, $a$ = −4.2 m s$^{-2}$, $s$ = 1.0, and $d$ = 0.37. Red and green lines show the shock locations for the model shocks extracted using the $\alpha$ method with the 4 stream solar wind model and the $a$ method with the 1 stream solar wind model, respectively. Parameters are: $v_i$ = 1369 km s$^{-1}$, $a$ = −6.1 m s$^{-2}$, $s$ = 0.8, and $d$ = 0.10 (red), and $v_i$ = 1335 km s$^{-1}$, $a$ = −5.7 m s$^{-2}$, $s$ = 1.1, and $d$ = 0.01 (green). Note that the blue and green lines have merged for $t$ = 500 min and for $t$ = 2000 min.

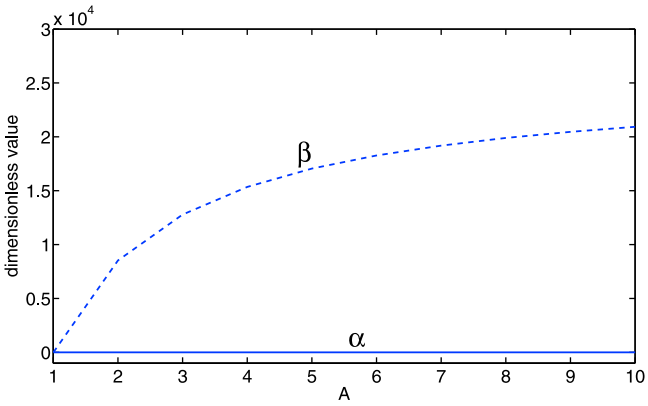


**Figure 5.** Effect on the assessment parameters $\alpha$ and $\beta$ of changing the relative flux levels by a multiplicative factor $A$.

increasing it at nonzero points of the two data sets. As these differences in relative flux level decrease, $\beta$ decreases monotonically toward its global minimum. The $\beta$ parameter is therefore shown to work best for data sets that differ in relative flux levels only.

[29] To investigate the effect of identical dynamic spectra features occurring at different times and frequencies, we again start with the four stream solar wind dynamic spectra $DB_T(t, f)$ (Figure 3, top right). Now we translate the spectrum by $O$ bins in time (moves $O$ min) and $O$ bins in frequency (moves $O$ frequency channels), and calculate $\alpha$ and $\beta$. For $O$ running from 1 to 50 we obtain Figure 6 which shows the effect on $\alpha$ and $\beta$. Translating the two images in time and frequency clearly has significant effects on both fitting parameters. The $\alpha$ parameter monotonically decreases as $O$ decreases and therefore will yield a quantity that can always be minimized to obtain better agreement. For most of the range of $O$, $\beta$ also decreases with decreasing $O$ toward the global minimum. However, $\beta$ does not decrease monotonically, showing the possibility of developing local minima that may affect parameter extraction because the system may converge to the wrong solution (i.e. not the global minimum). The $\alpha$ parameter is therefore more robust for data sets that are to be matched that differ by offsets in time and frequency.

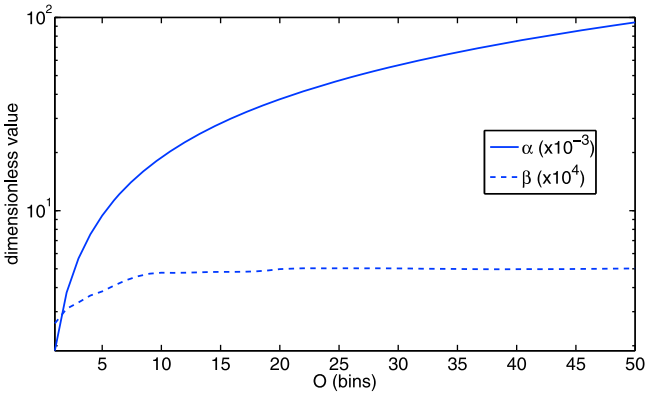


**Figure 6.** Effect on the assessment parameters $\alpha$ and $\beta$ of offsetting data by $O$ bins in both time and frequency.

### 5.2. Qualitative Effects of Different Shock Parameters

[30] In this section we show the qualitative effect on the dynamic spectra of altering the shock parameters. By changing the parameters in (17), along with the initial speed and deceleration we may obtain differences in the resulting spectra like those investigated in section 5.1. *Knock et al.* [2003a] showed the direct relationship for an individual ripple between predicted flux levels and parameters such as the radius of curvature and flow velocity. We expect that a narrow shock will produce emission that is less intense and broadband as it will span fewer radio-loud areas of the solar wind. Its small radius of curvature leads to long quasi-parallel flanks, which are likely radio-quiet [*Knock et al.*, 2003b]. Conversely, a larger or more planar shock should produce emission at higher flux levels and with a broader range of frequencies due to it encountering more radio-loud regions of the solar wind [*Knock et al.*, 2003a]. Increasing the speed of a shock should affect the dynamic spectra in at least two ways: First, the increased difference between shock speed and the ambient solar wind speed $v_{SW}$ leads to higher fluxes [*Knock et al.*, 2003a]. Secondly, the time at which features occur in the dynamic spectra will shift with speed because of the change in drift rate.

[31] The effects on the dynamic spectra may be seen directly from simulations run with shock parameters that are variations on the canonical set in section 4. We simulate using the four-stream solar wind model whose spectrum contains more distinct bands and emission regions (Figure 3, top right) and allows us to visualize differences more easily.

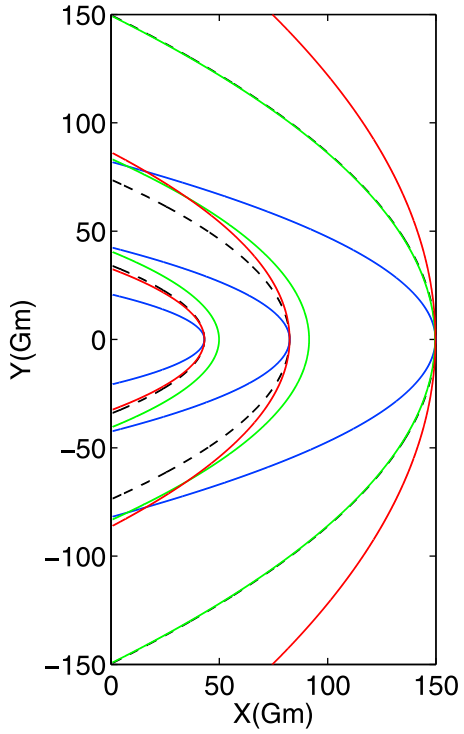


**Figure 7.** Shock locations at times $t$ = 500 min, $t$ = 1000 min, and $t$ = 2000 min from left to right for 4 model shocks. Broken black lines show the canonical shock, blue lines show the narrow model shock, red lines show the broad model shock, and green lines show the fast model shock.

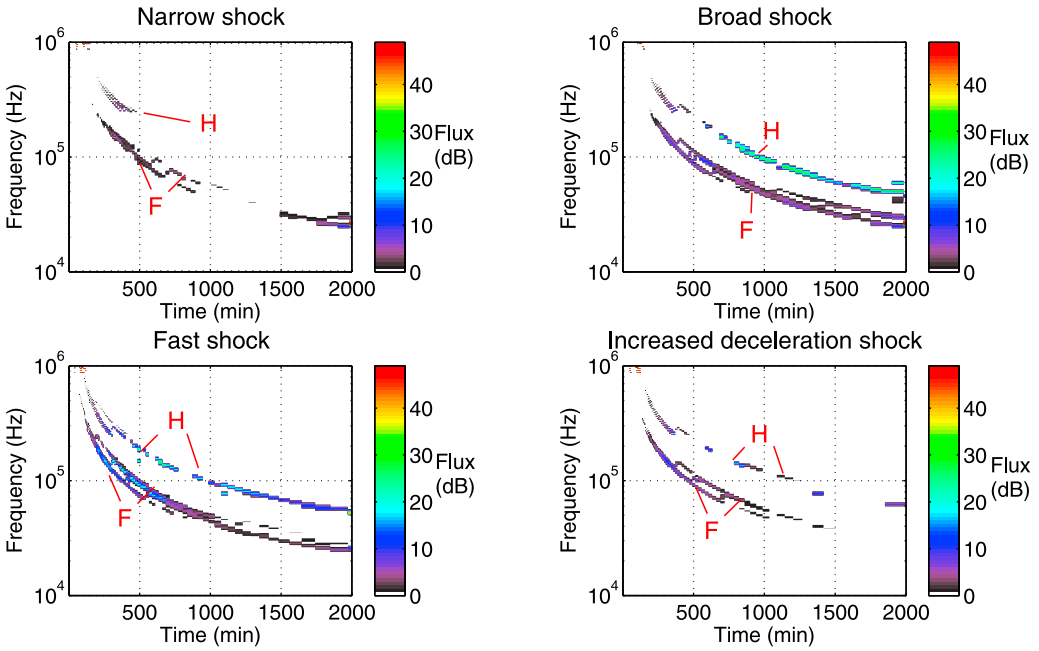


**Figure 8.** Dynamic spectra plotted on the same relative flux scale for the 4 model shocks with the fundamental (F) and harmonic (H) bands labeled: (top left) the narrow model shock; (top right) the broad model shock; (bottom left) the fast model shock; and (bottom right) the increased deceleration model shock. See text for shock parameters.

To represent a narrow shock of the same speed we choose $v_i$ = 1500 km s$^{-1}$, $a$ = −4.2 m s$^{-2}$, $s$ = 0.3, and $d$ = 0.2, plotted in blue in Figure 7. The dynamic spectrum is shown in Figure 8 (top left) and clearly shows much weaker bands of emission (around 10 dB lower) than those in Figure 3 (top right). Due to the low level of relative flux, many of the bands taper out earlier and begin later in time. Large regions of emission are missing from around 800 to 1400 min, especially apparent in the harmonic band. The remaining emission is indeed narrower in frequency span than the canonical simulation's prediction, as expected. We also note, as above in section 3.4, the differences between the fundamental and harmonic emission bands due to the different forms of (12) and (13).

[32] To simulate a large planar-like shock we choose $v_i$ = 1500 km s$^{-1}$, $a$ = −4.2 m s$^{-2}$, $s$ = 2.0, and $d$ = 1.0, plotted in red in Figure 7. We obtain the dynamic spectrum in Figure 8 (top right). Some of the patchy emission from the canonical parameter simulation (Figure 3, top right) has been replaced with more broad band, continuous, and intense emission. The changes are largest in the harmonic band where there is at least a 10 dB increase in relative flux after 500 min. The more broadband and intense emission found is consistent with expectations for a broader shock front.

[33] We simulate a fast shock with $v_i$ = 1800 km s$^{-1}$, $a$ = −9.2 m s$^{-2}$, $s$ = 1, and $d$ = 0.37, plotted in green in Figure 7. The resulting spectrum is shown in Figure 8 (bottom left). Since the simulation time window remains the same, the deceleration has increased from the canonical value of $a$ = −4.2 m s$^{-2}$ to $a$ = −9.2 m s$^{-2}$. The effects of this change in speed are subtle since most of the features appear similar to the original case. However, differences are seen in the steeper drift rate, especially noticeable at early times. This leads to the same features occurring at higher frequencies and up to around 100 min earlier. The strength of emission has also increased by around 10 dB, which is noticeable in the bright regions in the center of the main bands between 400 and 600 min. This simulation demonstrates the relationship between the shock's speed and the shifting of features in frequency, time, and intensity.

[34] Finally we test the effects of altering the shock's deceleration while keeping all other parameters fixed. The dynamic spectrum for the event modeled with $v_i$ = 1500 km s$^{-1}$, $a$ = −8 m s$^{-2}$, $s$ = 1.0, and $d$ = 0.37 is shown in Figure 8 (bottom right). Like the canonical spectrum, this spectrum also shows two sets of emission bands which agree well qualitatively until around 600 min. However, overall the emission is weaker, less continuous, and narrower than the canonical spectrum. This trend appears to become more apparent as time progresses, as the increased deceleration slows this shock's speed considerably and leads to weakened emission. The effects of the deceleration are also apparent in the smaller drift rate.

### 5.3. Quantitative Effect of Different Shock Parameters

[35] In this section we quantify the agreement between the canonical data set and the four chosen test cases of the narrow, broad, fast, and rapidly decelerating shock discussed in section 5.2. This is done by calculating the parameters $\alpha$ and $\beta$ using (20) and (21), where the canonical dynamic spectrum is $DB_O(t, f)$ in each case.

[36] For the agreement between the canonical parameter simulation and that for the narrow model shock we obtain $\alpha = 2.00 \times 10^{-3}$ with $(t_0, f_0)$ = (4, 0) and $\beta = 3.04 \times 10^4$. Using the broad model shock we obtain $\alpha = 8.30 \times 10^{-3}$ with $(t_0, f_0)$ = (8, 4) and $\beta = 2.60 \times 10^4$. Using the fast model shock we obtain $\alpha = 5.00 \times 10^{-3}$ with $(t_0, f_0)$ = (10, 0) and $\beta = 3.33 \times 10^4$. Finally, using the increased

**Table 4.** Summary of the Results for Extracting the Parameters for Each Model Shock[a]

| | Narrow | | | Broad | | | Fast | | | Increased Deceleration | | |
|---|---|---|---|---|---|---|---|---|---|---|---|---|
| | $v_i(\pm)$ | $s(\pm)$ | $d(\pm)$ | $v_i(\pm)$ | $s(\pm)$ | $d(\pm)$ | $v_i(\pm)$ | $s(\pm)$ | $d(\pm)$ | $v_i(\pm)$ | $s(\pm)$ | $d(\pm)$ |
| Input | 1500 | 0.3 | 0.37 | 1500 | 2.0 | 1.00 | 1800 | 1.0 | 0.37 | 1500 | 1.0 | 0.37 |
| $\alpha$ | 1453(21) | 0.6(0.1) | 0.70(0.03) | 1696(72) | 1.3(0.1) | 0.83(0.14) | 1757(39) | 1.2(0.1) | 0.39(0.03) | 1630(34) | 1.6(0.2) | 0.63(0.07) |
| $\beta$ | 1501(3) | 0.4(0.1) | 0.58(0.03) | 1500(4) | 2.0(0.1) | 0.94(0.01) | 1790(3) | 0.9(0.1) | 0.29(0.01) | 1499(3) | 1.1(0.1) | 0.22(0.03) |

[a]Each row lists, from left to right, the model shock parameters extracted for each of the four scenarios. Each column lists the correct input parameters, and those extracted using the $\alpha$ and $\beta$ assessment parameters, respectively.

deceleration model shock we obtain $\alpha = 2.5 \times 10^{-3}$ with $(t_0, f_0) = (5, 0)$ and $\beta = 2.45 \times 10^4$.

[37] The effects of changing the shock parameters on the quantitative merit parameters $\alpha$ and $\beta$ are as follows. First, to introduce time and frequency offsets to where the best agreement occurs, leading to nonzero values of $\alpha$ which increase as the offsets increase. Secondly, to alter the relative flux levels, thereby creating a nonzero difference in relative flux levels between the two data sets, and increasing the magnitude of $\beta$.

[38] The smallest value of $\alpha$ occurs for the case of the narrow shock. The narrowing of emission bands may be responsible for constraining the best match to occur with close to zero offsets between the data sets. Conversely the larger $\alpha$ value in the case of the broad shock may be due to the wide emission bands allowing emission to move to larger offsets and still match the features. The smallest value of $\beta$ occurs for the case of the increased deceleration model shock. Inspection of Figure 7 reveals that the main differences between the dynamic spectra for the increased deceleration and canonical model shocks occur at late times, while at early times the two dynamic spectra match closely with spectral features and emission levels. With large amounts of overlapping emission of a similar relative flux level, the $\beta$ value is noticeably decreased. These test cases confirm that simulated spectral features that do not resemble those in the input (or "observed") dynamic spectrum lead to a larger values of the assessment parameters.

[39] As an additional test of the optimization method, we attempt to extract the model shock parameters used to calculate the dynamic spectra in Figure 8. Again we use the four-stream solar wind model and a starting simplex

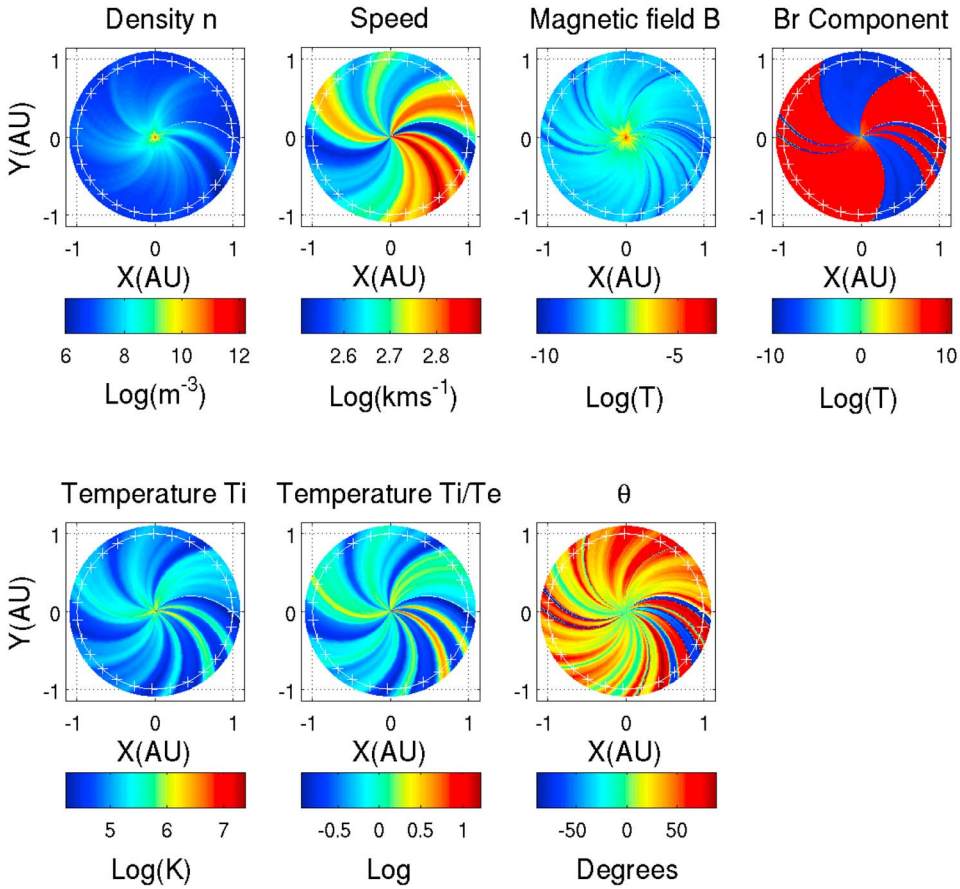


**Figure 9.** Data-driven solar wind model for the period 7 November to 3 December 2004, calculated using the technique of *Florens et al.* [2007] and Wind spacecraft data. $B_r$ is the radial magnetic field component with inward and outwards senses, and $\theta$ is the angle between **B** and the radial direction.

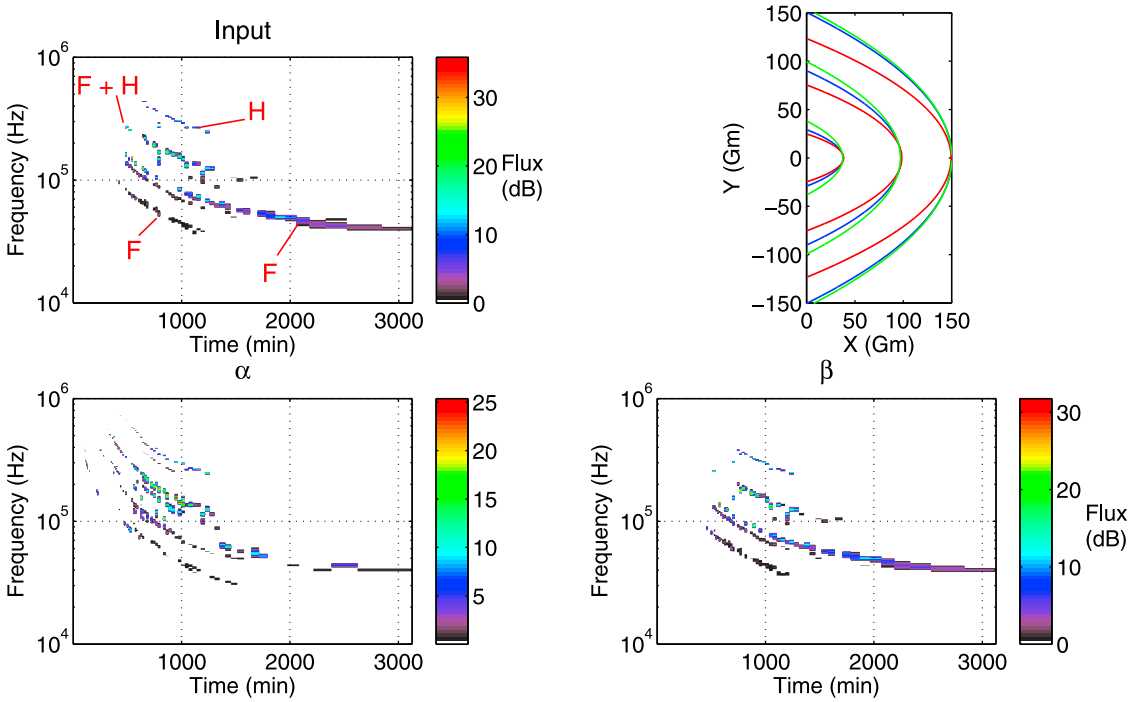


**Figure 10.** (top left) Input dynamic spectrum using the real structured solar wind in Figure 9 with the fundamental (F) and harmonic (H) emission labeled. (top right) Shock location and evolution at times $t$ = 500 min, $t$ = 1500 min, and $t$ = 3126 min from left to right. The blue lines show the input shock, the red dotted lines show the shock extracted using $\alpha$, and the green dotted lines show the shock extracted using $\beta$. Note that the red and blue lines have all but merged at $t$ = 500, and the blue and green lines have all but merged at $t$ = 3126 min. (bottom left) Dynamic spectrum extracted using $\alpha$. (bottom right) Dynamic spectrum extracted using $\beta$.

whose vertexes, like those in Table 2, surround the correct solution. The results of the parameter extractions are displayed in Table 4 and show good agreement with the input parameters. This demonstrates the method's ability to extract different solutions quite reliably and accurately, meaning specifically to within an average of 30% or better.

## 6. Extracting Shock Parameters With a Realistic Structured Model Solar Wind

[40] We now apply the minimization method to the recovery of shock parameters for a real structured solar wind. The data used to create the solar wind model, with the technique of *Florens et al.* [2007], were taken from the Wind spacecraft for the period 6 November 2004 until 2 December 2004. The resulting solar wind model is plotted in Figure 9. We simulate using the parameters $v_i$ = 1350 km s$^{-1}$, $a$ = −5.8 m s$^{-2}$, $s$ = 1.0, $d$ = 0.00, which are actual estimates for a CME driven shock leading to Figure 1's type II event on 3 December 2004 (D. Hillan et al., submitted manuscript, 2011). The dynamic spectrum predicted for these parameters is shown in Figure 10 (top left) and the starting vertex for the Amoeba routine is shown in Table 2. The spectrum shows two main bands of emission, the lower being fundamental (F), and the higher the harmonic (H) counterpart. Based on inspection of Figure 9, the contribution to the upper band from fundamental emission is likely sourced from a neighboring radio-loud solar wind stream with higher density, low solar wind speed and close to Earth (the blue region with $X > 0$ and $Y \approx 0$). Furthermore, the very weak low frequency harmonic bands and high frequency fundamental bands with differing drift rates are likely a contribution from a more distant source region with lower and higher densities streams, respectively. The predicted dynamic spectra may be compared directly with the observed type II event shown in Figure 1. Preliminary comparisons by eye are promising and the quantitative analyses are performed by D. Hillan et al. (submitted manuscript, 2011).

[41] The results of the minimizations for the three free parameters ($v_i$, $s$, and $d$) are shown in Table 5. The two resulting dynamic spectra are plotted in Figure 10 (bottom left and right). For this example, the extracted shock parameters are more accurate that in the tests of earlier Sections when minimizing both $\alpha$ and $\beta$. It appears as though the increased complexity of the model solar wind and resulting dynamic spectra has led to fewer possible solutions or local minima in the parameter space. The minimization processes converge to shock parameters within 10% on average of the correct values, specifically: $v_i$ = 1369 ± 7 km s$^{-1}$ and 1335 ± 2 km s$^{-1}$ for an input of $v_i$ = 1350 km s$^{-1}$, $s$ = 0.8 ± 0.1 and $s$ = 1.1 ± 0.1 for an input of $s$ = 1.0, and $d$ = 0.10 ± 0.01 and $d$ = 0.01 ± 0.01 for an input of $d$ = 0.00, for the $\alpha$ and $\beta$ minimizations, respectively.

[42] Figure 10 (top right) plots snapshots of the evolving model shock solutions extracted using the $\alpha$ and $\beta$ parameters in red and green, respectively. When compared with

**Table 5.** Amoeba Results for the Structured Solar Wind Model Using the Two Assessment Parameters[a]

| | Parameters | | | | Results | | | |
|---|---|---|---|---|---|---|---|---|
| Method | $v_i$ | $a$ | $s$ | $d$ | $C_{max}$ | $(t_0, f_0)$ | $\alpha$ | $\beta$ |
| $\alpha$ | $1369 \pm 7$ | $-6.1$ | $0.8 \pm 0.03$ | $0.10 \pm 0.01$ | 0.24 | (2,0) | $6.40 \times 10^{-4}$ | $4.95 \times 10^{4}$ |
| $\beta$ | $1335 \pm 2$ | $-5.7$ | $1.1 \pm 0.02$ | $0.01 \pm 0.01$ | 0.70 | (4,0) | $1.30 \times 10^{-3}$ | $1.56 \times 10^{4}$ |

[a]Each row lists from left to right the assessment parameter used, the parameters extracted, and the values of each assessment parameter.

the correct solution (blue line) it can be seen the relatively large value of $d$ in the shock solutions is unimportant and both methods are able to reproduce a model shock that tracks the input shock, especially near the shock nose. The offsets in time (compared with the event duration) and frequency are also relatively small i.e. the $\alpha$ method yields $(t_0, f_0) = (2, 0)$ and the $\beta$ method yields $(t_0, f_0) = (4, 0)$ which equates to much less than a 1% offset in time. The extracted dynamic spectra for the two solutions shown in Figure 10 (bottom left and right) are consistent with the inferrance that while the $\alpha$ method focuses on matching up the spectral features with minimal offsets, the $\beta$ solution focuses on matching the relative flux levels of the bulk of the emission.

[43] It is worth noting that the transition from the zero (isotropic), one, and four stream solar wind models in Section 4 (Figure 2) to the structured solar wind model in this Section, naturally develops fractured, bursty, and multiple lane features in the dynamic spectra. This shows that (1) the solar wind model is of large importance when attempting to accurately simulate a type II event, (2) the direction the shock propagates (here assumed Earthward) is likely to be important, as changes in direction will move the source region to parts of the solar wind with different plasma parameters, and (3) having multiple active source regions on the shock can plausibly generate split band-like emissions similar to those observed, removing the need for such structure to be interpreted in terms of downstream emission [*Cairns*, 2011].

## 7. Discussion and Conclusions

[44] In this paper we have summarized the current theoretical model for type II bursts and its extension to include a data-driven solar wind model. For the first time the appropriate radio background has been included in order to make direct comparisons with the WIND/WAVES observations. In order to make quantitative comparisons, we introduced parameters $\alpha$ and $\beta$ to assess the agreement between type II dynamic spectra, whether modeled or observed. The $\alpha$ parameter was shown to robustly extract parameters when features in the spectra are shifted in time and frequency only and was only weakly dependent on the absolute magnitudes, whereas the $\beta$ parameter is more successful in matching relative flux levels in the bulk of the emission.

[45] The parameter extraction method was applied to type II dynamic spectra calculated for artificial solar wind models ranging from featureless (isotropic) to four streams. The method successfully recovered the input shock parameters to within 30% or better, even as the complexity of the wind was increased. Furthermore the effect of varying shock parameters on both the qualitative appearance of the simulated dynamic spectra, and on the quantitative assessment parameters $\alpha$ and $\beta$ was investigated. Varying the initial shock speed or deceleration led to changes in intensity and drift rate, while varying the shock's size $s$ and expansion index $d$ mainly controlled the frequency width of the emission and led to narrow or broad emission bands. Four sets of shock parameter that modeled a broad, narrow, fast and increased deceleration shock were successfully extracted from the four-stream solar wind model using both the $\alpha$ and $\beta$ assessment parameters with an average accuracy of 30%.

[46] Finally the method was tested on a real structured solar wind with realistic CME shock parameters using both the $\alpha$ and $\beta$ assessment parameters. The method was successful in extracting the parameters of the artificially created type II event to within an accuracy of around 10% percent. The speed $v_i$ and size $s$ were recovered more accurately than the expansion index $d$, but even so the shock parameters extracted led to time-varying positions of the model shocks that very closely resemble that of the artificial events. This demonstrates a weak dependence on the expansion index $d$ in these cases. In future revisions of the theory perhaps the parameters $s$ and $d$ may be somehow combined into a single parameter to describe a more general shock with fewer free parameters. Furthermore, the model shocks investigated here have the nose of the shock propagating directly toward Earth. Altering the shock's direction with respect to Earth will affect the flux seen at a distant observer as the distance to the source region may increase and the line of sight from the source region to the observer may be obscured by the shock itself (so-called frequency blocking) [*Cairns and Knock*, 2006]. Investigating the effect of an additional direction parameter represents a possible future extension of the model.

[47] The results presented here pave the way for the method to be applied to real observed type II radio bursts. The companion paper (D. Hillan et al., submitted manuscript, 2011) applies the method to produce the first quantitative data-theory comparisons for interplanetary type II bursts. Note that maximizing the agreement between the observed type IIs and those simulated using our theory and methods will allow us to constrain shock parameters and to test the theory. This has important applications to space weather predictions. We believe that similar analyses could be applied to STEREO/WAVES data of future type II events in order to obtain shock parameters and so predict if, when, and how CME shocks will impact Earth's magnetosphere.

[48] **Acknowledgments.** Philippa Browning thanks the reviewers for their assistance in evaluating this paper.

## References

Bale, S. D., M. J. Reiner, J.-L. Bougeret, M. L. Kaiser, S. Krucker, D. E. Larson, and R. P. Lin (1999), The source region of an interplanetary type II radio burst, *Geophys. Res. Lett.*, *26*, 1573.

Bougeret, J., et al. (1995), WAVES: The radio and plasma wave investigation on the Wind spacecraft, *Space Sci. Rev.*, *71*, 231.
Cairns, I. H. (1986), The source of free energy for type II solar radio bursts, *Proc. Astron. Soc. Aust.*, *6*, 444.
Cairns, I. H. (1987a), A theory for the Langmuir waves in the electron foreshock, *J. Geophys. Res.*, *92*, 2329.
Cairns, I. H. (1987b), The electron distribution function upstream from the Earth's bow shock, *J. Geophys. Res.*, *92*, 231.
Cairns, I. H. (1988), A semiquantitative theory for the 2f(p) radiation observed upstream from the Earth's bow shock, *J. Geophys. Res.*, *92*, 2329.
Cairns, I. H. (2011), Coherent radio emissions associated with solar system shocks, in *The Sun, the Solar Wind, and the Heliosphere*, *IAGA Spec. Sopron Book Ser.* vol. 4, edited by M. P. Miralles and J. S. Almeida, p. 267, Springer, Dordrecht, Netherlands.
Cairns, I. H., and S. A. Knock (2006), Predictions for dynamic spectra and source regions of type II radio bursts in the homogenous corona and solar wind, in *Planetary Radio Emissions VI*, edited by H. O. Rucker, W. S. Kurth, and G. Mann, p. 419, Ost. Akad. Wissenchaften, Vienna.
Cairns, I. H., and D. B. Melrose (1985), A theory for the 2fp radiation upstream of the Earth's bow shock, *J. Geophys. Res.*, *90*, 6637.
Cairns, I. H., and P. A. Robinson (1999), Strong evidence for stochastic growth of Langmuir-like waves in Earth's foreshock, *Phys. Rev. Lett.*, *82*, 3066.
Cairns, I. H., S. A. Knock, P. A. Robinson, and Z. Kuncic (2003), Type II solar radio bursts: Theory and space weather implications, *Space Sci. Rev.*, *107*, 27.
Cairns, I. H., V. V. Lobzin, A. Warmuth, B. Li, P. A. Robinson, and G. Mann (2009), Direct radio probing and interpretation of the Sun's plasma density profile, *Astrophys. J. Lett.*, *706*, L265.
Cane, H. V. (1985), The evolution of interplanetary shocks, *J. Geophys. Res.*, *90*, 191.
Cane, H. V., and W. C. Erickson (2005), Solar type II radio bursts and IP type II events, *Astrophys. J.*, *623*, 1180.
Cane, H. V., R. G. Stone, J. Fainberg, J. L. Steinberg, and S. Hoang (1982), Type II solar radio events observed in the interplanetary medium, I, General characteristics, *Sol. Phys.*, *78*, 187.
Cane, H. V., N. R. Sheeley Jr., and R. A. Howard (1987), Energetic interplanetary shocks, radio emission, and coronal mass ejections, *J. Geophys. Res.*, *92*, 9869.
Claßen, H. T., and H. Aurass (1999), On the association between type II radio bursts and CMEs, *Astron. Astrophys.*, *384*, 1098.
Cliver, E. W., D. F. Webb, and R. A. Howard (1999), On the origin of solar metric type II bursts, *Sol. Phys.*, *187*, 89.
Dulk, G. A., Y. Leblanc, and J. Bougeret (1999), Type II shock and CME from the corona to 1 AU, *Geophys. Res. Lett.*, *26*, 2331.
Ergun, R. E., et al. (2008), Eigenmode structure in solar-wind Langmuir waves, *Phys. Rev. Lett.*, *101*, 051101, doi:10.1103/PhysRevLett.101.051101.
Filbert, P. C., and P. J. Kellogg (1979), Electrostatic noise at the plasma frequency beyond the Earth's bow shock, *J. Geophys. Res.*, *84*, 1369.
Florens, M. S. L., I. H. Cairns, S. A. Knock, and P. A. Robinson (2007), Data-driven solar wind model and prediction of type II bursts, *Geophys. Res. Lett.*, *34*, L04104, doi:10.1029/2006GL028522.
Gopalswamy, N., A. Lara, R. P. Lepping, M. L. Kaiser, D. Berdichevsky, and O. C. St. Cyr (2000), Interplanetary acceleration of coronal mass ejections, *Adv. Space Res.*, *27*, 145.
Gopalswamy, N., A. Lara, S. Yashiro, M. L. Kaiser, and R. A. Howard (2001), Predicting the 1-AU arrival times of coronal mass ejections, *J. Geophys. Res.*, *106*, 29,207.
Gopalswamy, N., A. Lara, P. K. Manoharan, and R. A. Howard (2004), An empirical model to predict the 1-AU arrival of interplanetary shocks, *Adv. Space Res.*, *36*, 2289.
Hillan, D. S., I. H. Cairns, P. A. Robinson, and A. Mohamed (2010), Prediction of background levels for the Wind WAVES instrument and implications for the galactic background radiation, *J. Geophys. Res.*, *115*, A06102, doi:10.1029/2009JA014714.
Hoang, S., C. Lacombe, R. J. MacDowall, and G. Thejappa (2007), Radio tracking of the interplanetary coronal mass ejection driven shock crossed by Ulysses on 10 May 2001, *J. Geophys. Res.*, *112*, A09102, doi:10.1029/2006JA011906.
Kim, E.-H., I. H. Cairns, and P. A. Robinson (2007), Extraordinary-mode radiation produced by linear-mode conversion of Langmuir waves, *Phys. Rev. Lett.*, *99*, 015003, doi:10.1103/PhysRevLett.99.015003.
Knock, S. A., and I. H. Cairns (2005), Type II radio emission predictions: Sources of coronal and interplanetary spectral structure, *J. Geophys. Res.*, *110*, A01101, doi:10.1029/2004JA010452.
Knock, S. A., I. H. Cairns, P. A. Robinson, and Z. Kuncic (2001), Theory of type II solar radio emission from the foreshock region of an interplanetary shock, *J. Geophys. Res.*, *106*, 25,041.
Knock, S. A., I. H. Cairns, P. A. Robinson, and Z. Kuncic (2003a), Theoretically predicted properties of type II radio emission from an interplanetary foreshock, *J. Geophys. Res.*, *108*(A3), 1126, doi:10.1029/2002JA009508.
Knock, S. A., I. H. Cairns, and P. A. Robinson (2003b), Type II radio emission predictions: Multiple shock ripples and dynamic spectra, *J. Geophys. Res.*, *108*(A10), 1361, doi:10.1029/2003JA009960.
Kuncic, Z., I. H. Cairns, and S. A. Knock (2002), Analytic model for the electrostatic potential jump across collisionless shocks, with application to Earth's bow shock, *J. Geophys. Res.*, *107*(A8), 1218, doi:10.1029/2001JA000250.
Lobzin, V. V., I. H. Cairns, and P. A. Robinson (2009), Evidence for wind-like regions, acceleration of shocks in the deep corona, and relevance of 1/f dynamic spectra to coronal type II bursts, *Astrophys. J. Lett.*, *677*, L129.
Lobzin, V. V., I. H. Cairns, P. A. Robinson, G. Steward, and G. Patterson (2010), Automatic recognition of coronal type II radio bursts: The Automated Radio Burst Identification System method and first observations, *Astrophys. J. Lett.*, *710*, L58.
Maksimovic, M. V., V. Pierrard, and P. Riley (1997), Ulysses electron distributions fitted with Kappa functions, *Geophys. Res. Lett.*, *24*, 1151.
Malaspina, D. M., I. H. Cairns, and R. E. Ergun (2010), The 2fp radiation from localized Langmuir waves, *J. Geophys. Res.*, *115*, A01101, doi:10.1029/2009JA014609.
McLean, D. J. (1967), Band splitting in type II solar radio bursts, *Proc. Astron. Soc.*, *12*, 401.
Melrose, D. B. (1985), *Instabilities in Space and Laboratory Plasmas*, Cambridge Univ. Press, New York.
Nelder, J. A., and R. Mead (1965), A simplex method for function minimization, *Comput. J.*, *7*, 308.
Nelson, G. J., and D. B. Melrose (1985), Type II bursts, in *Solar Radiophysics*, edited by D. J. McLean and N. R. Labrum, p. 333, Cambridge Univ. Press, New York.
Neugebauer, M., and J. Giacolone (2005), Multispacecraft observations of interplanetary shocks: Nonplanarity and energetic particles, *J. Geophys. Res.*, *110*, A12106, doi:10.1029/2005JA011380.
Press, W. H., S. A. Teukolsky, W. T. Vetterling, and B. P. Flannery (Eds.) (1992), *Numerical Recipes in FORTRAN. The Art of Scientific Computing*, 2nd ed., Cambridge Univ. Press, New York.
Reiner, M. J., M. L. Kaiser, J. Fainberg, and R. G. Stone (1998), A new method for studying remote type II radio emissions from coronal mass ejection-driven shocks, *J. Geophys. Res.*, *103*, 29,651.
Reiner, M. J., M. L. Kaiser, and J.-L. Bougeret (2001), Radio signatures of the origin and propagation of coronal mass ejections through the solar corona and interplanetary medium, *J. Geophys. Res.*, *106*, 29,989.
Reiner, M. J., M. L. Kaiser, and J.-L. Bougeret (2007), Coronal and interplanetary propagation of CME/shocks from radio, in situ and white-light observations, *Astrophys. J.*, *663*, 1369.
Robinson, P. A. (1992), Clumpy Langmuir waves in type III radio sources, *Sol. Phys.*, *139*, 147.
Robinson, P. A., and I. H. Cairns (1993), Stochastic growth theory of type II solar radio emission, *Astrophys. J.*, *418*, 506.
Robinson, P. A., and I. H. Cairns (1998a), Fundamental and harmonic emission in type III solar radio bursts. Part I: Emission at a single location or frequency, *Sol. Phys.*, *181*, 363.
Robinson, P. A., and I. H. Cairns (1998b), Fundamental and harmonic emission in type III solar radio bursts. Part II: Dominant modes and dynamic spectra, *Sol. Phys.*, *181*, 395.
Robinson, P. A., and I. H. Cairns (2000), Theory of type III and type II solar radio emission, in *Radio Astronomy at Long Wavelengths*, *Geophys. Monogr. Ser.*, vol. 119, edited by R. Stone, E. Weiler, and M. Goldstein, p. 37, AGU, Washington, D. C.
Robinson, P. A., I. H. Cairns, and D. A. Gurnett (1993), Clumpy Langmuir waves in type III radio sources: Comparison of stochastic-growth theory with observations, *Astrophys. J.*, *407*, 790.
Schmidt, J. M., and N. Gopalswamy (2008), Synthetic radio maps of CME-driven shocks below 4 solar radii heliocentric distance, *J. Geophys. Res.*, *113*, A08104, doi:10.1029/2007JA013002.
Smerd, S. F., K. V. Sheridan, and R. T. Stewart (1974), On split-band structure in type II radio bursts from the Sun (presented by S.F. Smerd), in *Coronal Disturbances: Proceedings from IAU Symposium no. 57 held at Surfers Paradise, Queensland Australia, 7–11 September, 1973*, edited by G. Newkirk, p. 389, Int. Astron. Union, Dordrecht, Netherlands.
Vrsnak, B., J. Magdalenic, H. Aurass, and G. Mann (2002), Band-splitting of coronal and interplanetary type II bursts: Coronal magnetic field and Alven velocity, *Astron. Astrophys.*, *396*, 673.
Wild, J. P. (1950a), Observations of the spectrum of high-intensity solar radiation at metre wavelengths. II. Outbursts, *Aust. J. Sci. Res.*, *A3*, 399.

Wild, J. P. (1950b), Observations of the spectrum of high-intensity solar radiation at metre wavelengths. III. Isolated bursts, *Aust. J. Sci. Res.*, *A3*, 541.

Wild, J. P., S. F. Smerd, and A. A. Weiss (1963), Solar bursts, Annual review, *Astron. Astrophys.*, *1*, 291.

Yashiro, S., N. Gopalswamy, G. Michalek, O. C. St. Cyr, S. P. Plunkett, N. B. Rich, and R. A. Howard (2004), A catalog of white light coronal mass ejections observed by the SOHO spacecraft, *J. Geophys. Res.*, *109*, A07105, doi:10.1029/2003JA010282.

Zarka, P., B. Cecconi, and W. S. Kurth (2004), Jupiter's low-frequency radio spectrum from Cassini/Radio and Plasma Wave Science (RPWS) absolute flux density measurements, *J. Geophys. Res.*, *109*, A09S15, doi:10.1029/2003JA010260.

I. H. Cairns, D. S. Hillan, and P. A. Robinson, School of Physics, University of Sydney, Sydney, NSW 2006, Australia. (hillan@physics.usyd.edu.au)